Electron vortex orbits and merger

T. B. Mitchell[a)]
Los Alamos National Laboratory, Los Alamos, New Mexico 87544

C. F. Driscoll[b)]
Department of Physics 0319, University of California at San Diego, La Jolla, California 92093-0319

Pure electron plasma columns are contained inside hollow conducting cylinders in an axial magnetic field. In the 2D **E×B** drift approximation, an electron column is a vortex evolving in (r, θ) according to the Euler equation. First the center-of-mass orbits of two vortices sufficiently well-separated to be stable to merger are characterized. Equilibria are observed in which the vortices orbit about the center of the cylinder, with either oscillations about stable equilibria or exponential divergence away from unstable equilibria. The equilibrium positions, oscillation frequencies, and instability rates for these spatially extended vortices agree well with the predictions of point vortex theory, apparently because surface waves and shape distortions do not couple significantly to the center-of-mass motion. Next, the merger of two vortices with unequal radii is quantified. Merger is accompanied by the formation of filamentary arms, and results ultimately in an axisymmetric central core surrounded by a lower density halo. The self-energy of the merged core is found to be roughly the sum of the self-energy of the merging vortices. The fraction of the total circulation entrained into the core varies from 70% to 90% as the ratio of the initial vortex radii is varied from 1:1 to 2:1. The point-like vortex dynamics and the circulation loss with merger are both consistent with the ''punctuated Hamiltonian'' models of decaying turbulence. © *1996 American Institute of Physics.* [S1070-6631(96)00307-8]

I. INTRODUCTION

This work presents the results of experiments on electron vortices, which are electron plasma columns contained inside a trap consisting of hollow conducting cylinders in a uniform axial magnetic field. In the operating regime of the experiments, where fast electron motions in the axial direction average over axial variations and the 2D **E×B** drift approximation is valid, the columns evolve according to the 2D Euler equation. The columns therefore evolve as would 2D columns of vorticity in an incompressible and inviscid fluid contained in a circular tank. The vorticity of the flow is proportional to the electron density, with the sign of the vorticity given by the sign of the charge.[1,2]

There are several advantages to using electron plasmas, rather than conventional fluids, to study vortex dynamics. For example, in the electron system there is no boundary layer at the wall to complicate the dynamics, and the dissipation is very low: An electron vortex centered within the trap will rotate about its axis over 10^5 times before its radius doubles due to ''viscous'' effects. Additionally, the vorticity is easily manipulated, accurately measured and directly imaged.[2]

The dynamics of 2D vortices has been studied for over 100 years, due to the central role of vorticity in fluid dynamics and turbulence. Experiments and simulations have established that vortices can emerge from both laminar flows[3] and structureless initial conditions.[4] The subsequent evolution of these systems can be dominated by the dynamics of the vortices, which includes merger of like-signed vortices, mutual advection, and vortex symmetrization.

Recent studies of this many-vortex state, using direct numerical simulations of the Navier-Stokes equations, have supported the hypothesis that the essential features of the evolution are contained in a simple ''punctuated Hamiltonian'' model.[5,6] In the punctuated Hamiltonian model, the motions of the spatially extended vortices are calculated by the point vortex approximation, and simple rules are used to replace two vortices with one bigger vortex when they approach close enough to merge. These models have resulted in predictions for timescales which are in qualitative agreement with the results of simulations.[5–7] However, the assumptions of the punctuated Hamiltonian model have not previously been tested by detailed studies (experimental or theoretical) of the dynamics of spatially extended vortices, or of asymmetric vortex merger. On the contrary, recent contour dynamics simulations of asymmetric vortex merger[8] found that the conditions for and the results of merger are substantially different than has been assumed in the punctuated Hamiltonian models.

This paper presents the results of experiments on electron vortices, with a focus on the punctuated Hamiltonian model. Because charge of only one sign can be contained by the trap at a given time, the experiments are necessarily of single-signed vortices. We first present studies of the (r, θ) drift motions of the ''center-of-vorticity'' of two vortices sufficiently well-separated so as to be stable to merger. Equilibria are observed in which the vortices orbit about the center of the cylinder, with either oscillations about stable equilibria or exponential divergence away from unstable equilibria.[9,10] The equilibrium positions, oscillation frequencies, and instability rates are obtained with high accuracy.

[a)]Electronic mail: tmitchell@lanl.gov
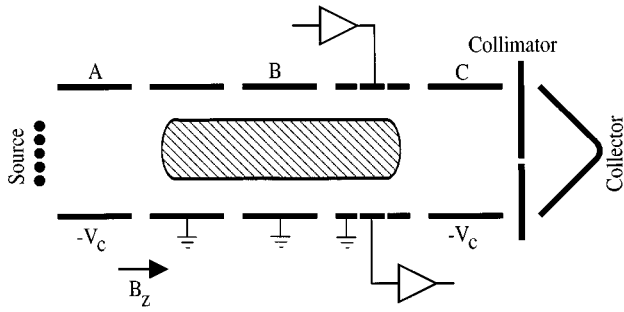[b)]Electronic mail: fdriscoll@ucsd.edu

FIG. 1. Schematic of the cylindrical confinement geometry.

We find that these results agree closely with predictions of point vortex theory, where the spatially extended vortices are replaced with point vortices of the same circulation. The wide-ranging agreement between experiments and point vortex theory suggests that surface waves and shape distortions do not couple significantly to these center-of-vorticity motions, at least at the precision of the current measurements.

Merger of two identical vortices has been previously studied in these electron traps.[11] The vortices do not merge in 10^4 orbits when they are initially separated by more than 1.6 diameters, but merge in 1 orbit time when separated by slightly less. Here, we study the merger of two vortices with different radii, but equal peak vorticity. The two vortices merge rapidly when they are closer than a critical separation, but stay separated for many orbits when the separation is slightly larger.[9] Merger is accompanied by the formation of filamentary arms, and results ultimately in an axisymmetric central core surrounded by a low density halo. The peak vorticity of the merged core is observed to be roughly the same as that of the merging vortices. The vorticity profile of the core and halo, and the lifetimes of the two-vortex state, are observed to be dependent on the initial placement of the two vortices.

The halo is defined to be that part of the merged profile sufficiently far away from the core that it is not bound, i.e., far enough that subsequent encounters with other vortices can advect it away. This suggests an operational definition for the halo as that part of an extended vortex which is more than 1.6 radii away from its center. Here, the vortex radius is defined by a radially-weighted integral out to the radius of the halo. Using this definition, we find that the fraction of the total circulation entrained into the central core after a merger varies from 70% to 90%, as the initial vortex radii are varied from 1:1 to 2:1. Additionally, the self-energy of the merged core is found to be roughly the same as the sum of the self-energy of the merging vortices. The quantitative picture of asymmetric merger which emerges from the experiments is consistent with ''punctuated Hamiltonian'' models of decaying turbulence, supported by direct numerical simulations of the Euler equations,[5,6] but differs substantially with results obtained from contour dynamics simulations.[8]

II. APPARATUS AND EXPERIMENTAL TECHNIQUES

The pure electron plasmas are contained in grounded conducting cylinders, as shown in Fig. 1. A uniform axial magnetic field (nominal $\mathbf{B}_z = 470$ G) provides radial confinement, and negative voltages applied to end cylinders provide axial confinement. Because Malmberg pioneered use of these traps to study plasma processes,[12] whereas Penning used a similar geometry to make a cold cathode ionization gauge,[13] we refer to the containment device as a ''Malmberg–Penning'' trap.

The apparatus is operated in an inject/manipulate/dump cycle. For injection, the left-most cylinder is briefly grounded, allowing electrons to enter from the negatively biased tungsten filament source. The filament bias determines the radius of the injected column, whereas the voltage drop across the filament determines the injected plasma density.[12] The trapped electrons can be contained for hundreds of seconds (about 10^6 turnover times), and can be manipulated in a variety of ways. Typically, we manipulate the plasma to create the desired initial condition, and then study the resulting evolution.

At any time t during this evolution, we can obtain the plasma density by grounding the right-most cylinder, thereby dumping the plasma. We measure the charge $Q(r,\theta,t)$ that flows along $\mathbf{B}_z$ through a collimator hole of area $A_h = \pi (1.6$ mm$)^2$, giving the z-averaged density $n(r,\theta,t)$ of a column of axial length L_p:

$$n(r,\theta,t) \equiv \int dz \, \frac{\widetilde{n}(r,\theta,z,t)}{L_p} = \frac{Q(r,\theta,t)}{-eA_hL_p}. \quad (1)$$

Only one density measurement is obtained from each machine cycle, and the evolution of $n(r,\theta,t)$ is obtained from multiple measurements. We obtain the temporal dependence by varying the evolution time t, and the spatial dependence by varying the position r of the radially scanning collimator hole and the phase θ of the initial condition. This imaging process relies on a high cycle-to-cycle reproducibility in the plasma initial conditions; typically we have less than 0.1% variations in the measured charge at a given point and time.

The plasma columns (''electron vortices'') considered here have densities $n \approx 2-5 \times 10^6$ cm^{-3} out to a radius $R_v \approx 0.4-2$ cm over a length $L_p \approx 20$ cm, and are contained within a wall of radius $R_w = 3.81$ cm. The electrons have a characteristic thermal energy $kT \approx 1$ eV, and create a space charge potential of about 5 V.

The plasma column can also be diagnosed and manipulated using isolated 60° sectors of the wall as antennas. Any azimuthal or axial variations in the electron density will induce variations in the image charges in the wall sectors, and thus waves can be detected with high sensitivity. Conversely, voltages applied to the wall sectors induce $\mathbf{E} \times \mathbf{B}$ drifts in the electrons, thereby launching waves or moving the center-of-mass. Applied voltages of ≥ 1 V can induce significant (i.e., readily detected) density waves in about 1 μs. Alternately, smaller voltages may be applied phase coherent with an internal wave using standard feedback techniques over larger times.

The electron column is easily manipulated in the axial direction by varying the containment voltages on various cylindrical electrodes. There are actually eight containment cylinders, as opposed to the five shown schematically in Fig. 1. A symmetric two-vortex initial condition is created by

Phys. Fluids, Vol. 8, No. 7, July 1996

T. B. Mitchell and C. F. Driscoll   1829

drifting a trapped column a distance R_1 off center, cutting it in half axially with a negative voltage on cylinder B, drifting one column to a new radial distance R_2, adjusting the relative θ-positions of the two columns, and then re-expanding the two columns axially. Alternately, an asymmetric two-vortex initial condition can be created by injecting a new column with a different radius after the first column is cut.

III. ELECTRON DYNAMICS

A. 2D guiding center fluid

The motion of the electrons in the magnetic field is well approximated by 2D guiding center theory. A thermal electron bounces axially along the magnetic field at a rate $f_b \equiv (kT/m)^{1/2}/2L_p \approx 10^6$ Hz. This rapid axial motion averages over any z-variations, allowing a 2D approximation of the system. Of course, averaged over all the electrons, there is no net motion in z. The thermal velocities perpendicular to B_z result in small orbits around the magnetic field lines, with cyclotron frequency $f_c \equiv eB/2\pi mc = 1.3 \times 10^9$ Hz and typical cyclotron radii $R_c \equiv (kT/m)^{1/2}/2\pi f_c = 50$ μm. (In this paper, upper case R will refer to radii in cm, and lower case r will refer to scaled radii, e.g., $r_c = R_c/R_w$.) Small r_c and large f_c allow the (r,θ) motion of an electron to be approximated by the position and velocity of its ''guiding center'' and $n(r,\theta)$ represents the density of guiding centers.

In the presence of an electric field perpendicular to B_z, the guiding centers drift with a velocity $v = c\mathbf{E} \times \mathbf{B}/B^2$. These electric fields arise from the unneutralized electron charges, and the electrostatic potential is readily obtained from Poisson's equation,

$$\nabla^2 \phi = 4\pi en, \tag{2}$$

together with the boundary condition $\phi(R_w, \theta) = 0$. Thus, the electrons drift with velocity

$$\mathbf{v}(r,\theta,t) = -c\nabla\phi \times \hat{\mathbf{z}}/B_z. \tag{3}$$

This velocity field is well defined even where there are no electrons. Taking the curl of the velocity gives the vorticity ζ:

$$\zeta \equiv \nabla \times \mathbf{v} = \nabla^2 \phi \frac{c}{B} = n\frac{4\pi ec}{B}. \tag{4}$$

The vorticity of the velocity field is thus proportional to the electron density. Using this fact, the continuity equation is also a statement that the convective derivative of the vorticity is zero, which is the evolution equation for the system:

$$\frac{\partial \zeta}{\partial t} + \mathbf{v} \cdot \nabla \zeta = 0. \tag{5}$$

The evolution of this 2D drift system is constrained by three ''robust'' conserved quantities.[2,14] These are the total number (line density) of particles,

$$N_L \equiv R_w^2 \int \int d\theta r dr n(r,\theta,t); \tag{6}$$

the angular momentum,

$$P_\theta \equiv R_w^4 \int \int d\theta r\ dr \left(\frac{-eB}{2c} r^2 \right) n(r,\theta,t); \tag{7}$$

and the electrostatic energy,

$$H_\phi \equiv R_w^2 \int \int d\theta r\ dr \left(-\frac{1}{2} e\phi(r,\theta,t) \right) n(r,\theta,t). \tag{8}$$

These quantities are all per unit axial length in a 3D system. Additionally, infinitely many ''ideal'' invariants, such as the integral of any power of n, exist; but these are not well conserved experimentally.

The 2D drift-Poisson equations (2)–(5) are isomorphic to the 2D Euler equations for an inviscid fluid of uniform density ρ. The electric potential ϕ is analogous to the stream function ψ, and the guiding center drift velocity v corresponds to the fluid velocity. The momentum equation for fluids gives an evolution equation (the vorticity equation[15]) for the system which is the same as Eq. (5). The boundary conditions are also equivalent, namely $\phi = $ const and $\psi = $ const on the walls. The wall boundary condition for electrons is truly free-slip: $v_\theta \neq 0$ at $R = R_w$, since the radial electric field is non-zero at the wall. In contrast, many liquids would require $v_\theta = 0$ at $R = R_w$, resulting in a turbulent boundary layer and a net viscous drag on the system. Thus, neglecting wall interactions, an initial distribution of electrons $n(r,\theta)$ in a cylinder, having vorticity $\zeta \propto n$, will evolve the same as an identical initial distribution of vorticity $\zeta(r,\theta)$ in a uniform inviscid 2D fluid. The same quantities will be conserved, with N_L, P_θ and H_ϕ known in fluids terminology as the total circulation, the total angular impulse, and the excess kinetic energy.[16]

B. Non-fluid effects

There are, of course, aspects of the 3D plasma system which are not within the framework of the 2D fluid analogy, and plasma parameters where the analogy does not hold. These can result in discrepancies between the observations and the predictions of 2D fluid theory. Two of the most important plasma effects are temperature-dependent finite length drifts and ''rotational pumping.''

1. Finite length effects

One well-known plasma effect with no fluid analogy is the drift which arises due to the confinement fields at the ends of the columns.[17–19] In some regimes, these drifts can be as large as those caused by space charge potential from the electron column. In the plasma parameter regime of this study, however, we find that these drifts result only in a dynamically unimportant shift of the rotational frame.

The shifts in frequency of a single vortex orbiting around the center of the trap (the $m = 1$ ''diocotron'' mode[17,18]) provides a good demonstration of finite length effects. Consider a z-independent column of line density N_L and radius R_v displaced a distance R from the axis of the containment walls. When the column remains circular, its field outside is that of a line charge (i.e., 2D point vortex) of circulation $\equiv \Gamma = (4\pi ec/B)N_L$ at radial position R, and the

T. B. Mitchell and C. F. Driscoll

image field is that of a line charge of opposite sign and the same N_L at radial position R_W^2/R. The electric field at the column center is then

$$\mathbf{E} = \frac{-2N_L e}{(R_w^2/R) - R}. \tag{9}$$

The force arising from the image field is $\mathbf{F} = -eN_L\mathbf{E}$, and the resultant drift velocity is

$$\mathbf{v} = \frac{c\mathbf{F}\times\mathbf{B}}{N_L e B^2}. \tag{10}$$

This gives the infinite length $m=1$ orbit frequency

$$f_{m=1}^{\infty} = \frac{c}{2\pi R}\frac{\mathbf{F}\times\mathbf{B}}{N_L e B^2} = \frac{cN_L e}{\pi B}\left[\frac{1}{R_w^2 - R^2}\right]. \tag{11}$$

Often, the prediction of Eq. (11) for $f_{m=1}^{\infty}$ differs substantially from the measured $m=1$ frequency $f_{m=1}$, because the end-confinement forces are substantial relative to the forces from the image field. A first-order model for the finite-length effects has been developed by Fine.[18] The important effect is a radial ''magnetron'' force which the electrostatic confinement fields exert in addition to, and proportional to, the axial confinement force. This radial force produces drifts in the θ-direction which, like the axial force needed to contain the column, will have a component proportional to the parallel temperature $T_\parallel$.

The magnetron force is, to first order in displacement, proportional to displacement. This is found to be true both of the model and of experimental results.[18] This proportionality suggests that finite-length effects will only produce an additional rotation of the column about the containment axis, at a constant frequency independent of R. Therefore the prediction of Fine's model is that the configuration will evolve as 2D vorticity would, only within a rotating frame produced by the magnetron motion.

We have experimentally tested whether this result, that finite-length effects produce only a constant frequency orbit in $\hat{\boldsymbol{\theta}}$, breaks down at large displacements. We find it to be valid for all the experimentally relevant displacements, i.e., $r \equiv R/R_w < 0.73$. We moved a narrow ($r_v = 0.15$) and cold ($T_\parallel \sim 0.25$ eV) column with an on-axis line density $N_L = 4.8\times10^6$ cm^{-1} to various displacements R, and measured $f_{m=1}$ and the off-axis line density N_L. The measured R and N_L were then used in Eq. (11) to calculate the infinite length frequency $f_{m=1}^{\infty}$, and the frequency shift from finite length effects was then $\Delta f_{m=1} = f_{m=1} - f_{m=1}^{\infty} \approx 1.2$ kHz.

We then repeated these measurements on a hotter ($T_\parallel \sim 2.0$ eV) and less dense ($N_L = 2.4\times10^6$ cm^{-1}) column. We plot $\Delta f_{m=1}$ versus R/R_w, for both the hot and cold column, in Fig. 2. No strong dependence of the frequency shifts on displacement in the region $0.36 < r < 0.73$ was found, and our conclusion is that to first order the fluid analogy is valid when all of the electron columns have the same $T_\parallel$. In the experiments of this paper, the initial conditions were adjusted so that this condition was met as well as possible ($\Delta T_\parallel / T_\parallel \lesssim 10\%$).

It is possible to change the plasma parameters such that temperature-dependent drifts become as large as the column
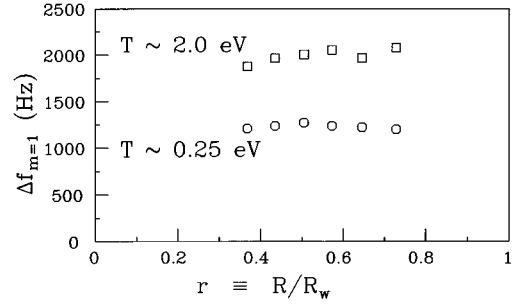

FIG. 2. Finite length frequency shift $\Delta f_{m=1}$ versus vortex position R for hot and cold electron columns.

self-rotation fluid drift. One would expect temperature drifts to shear a plasma column apart on a rotation timescale when the magnitude of the temperature-dependent velocity, v_e, is significantly larger than that of the fluid-like drift velocity, v_f. Peurrung and Fajans[19] have made a systematic experimental study of this effect. They defined a dimensionless parameter Λ equal to the ratio of the velocities,

$$\Lambda \equiv \frac{v_e}{v_f} = \kappa\frac{\lambda_D^2}{R_v L_p}, \tag{12}$$

where $\lambda_D \equiv (kT/4\pi e^2 n)^{1/2}$ is the plasma Debye length and κ is a parameter near unity. Deviations from fluid-like behavior was observed for $\Lambda \gtrsim 1$. They observed a fast smearing of the electron column when Λ was large, with the onset of smearing occurring in the regime $0.75 < \Lambda < 3.0$. We note that for the experiments discussed in this paper, $\Lambda < 0.1$ in all cases.

2. Rotational and orbital pumping

Electron columns in a Malmberg-Penning trap are subject to radial transport from asymmetries in the basically cylindrical trap,[20] but this occurs at rates too slow to impact the experiments of this paper. A faster transport process arises from the *apparent* asymmetry of the trap from the perspective of an off-axis vortex. For example, an off-axis column at $r = 0.4$ will expand at a rate about 10 times that of an on-axis column.[9] The effect responsible for this is ''rotational pumping,'' which has been extensively investigated experimentally by Cluggish and Driscoll[21] and theoretically by Crooks and O'Neil.[22]

The cause of rotational pumping is heating from interactions between the electrons and the confinement fields at the ends of the trap. In essence, the length of a ''flux tube'' of electrons depends on radial position. When a centered column rotates about the column center, all flux tubes remain at the same radius. However, if the column is not centered in the trap, column rotation will cause variations in the radial position of any flux tube, and the electrons experience small changes in their confinement lengths. This pumping, occurring at the rotation frequency of the column, serves to increase the plasma temperature.[23] This heating is at the expense of the column's electrostatic energy H_ϕ, and the column expands. Angular momentum is conserved in this process, so the column's center-of-mass moves towards the axis as the column expands, keeping P_θ constant.
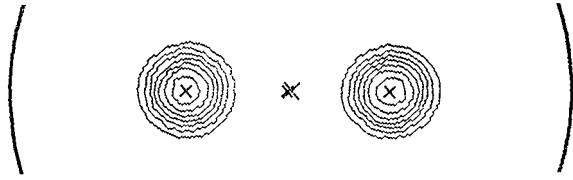
FIG. 3. Measured contours of z-integrated vorticity (or density) showing two vortices near the stable equilibrium orbit at $r_1 = r_2 = 0.36$. The outer arcs represent the wall at $r = 1$.
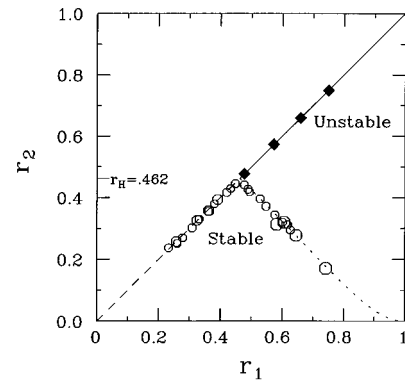

FIG. 4. Measured radial positions of stable (O) and unstable (diamond) equilibrium points, where $\theta_2 = \theta_1 + \pi$ for all points. The size of the symbol indicates the estimated uncertainty. The predictions of point vortex theory are also plotted for stable (dashes, dots) and unstable (solid line) equilibrium positions.

If there are other columns present in the trap, the column will also experience drifts due to their fields. Since excursions in R greater than $2R_v$ are possible from the orbits that the columns execute, column expansion can then occur at rates greater than those of rotational pumping. This phenomena has been termed ''orbital pumping,'' and its effects have been seen in measurements of two-vortex lifetimes,[9] as will be discussed below.

IV. ORBITS OF 2 EXTENDED VORTICES

In this section, we discuss the dynamics of nearly identical and well-separated (i.e., not merging) vortices. The electron vortices used here were relatively narrow (radius $r_v \sim 0.15$) hot ($T_\parallel \sim 1.8$ eV), and long ($L_p > 5R_w$). Their dynamics were investigated with two complementary diagnostics, wall sector signals and time series of $n(r, \theta)$ electron density plots. The density plots give direct measurements of vortex motions, but become too noisy to be useful about 500 μs after injection of the vortices (several orbit periods). The wall sector signals become interpretable about 400 μs after injection (the delay is due to a voltage spike caused by injection), but are limited in what they reveal of the motions.

We find that there exist equilibrium orbits in which each vortex orbits about the center of the cylinder at constant radius. Some of these equilibria are linearly stable, and others are unstable. We have measured both oscillations about stable equilibria and exponential divergence from unstable equilibria.[10] The measured equilibrium positions, oscillation frequencies, and instability rates are well predicted by treating the spatially extended vortices as if they were point vortices. The symmetric equilibria of 2 point vortices within a cylindrical boundary were first analyzed by Havelock;[24] we have extended this analysis to consider asymmetric equilibria.[9] Point vortex theory and the experiments both predict that the equilibrium orbits are unstable when the orbit radius is more than 0.46 times the wall radius. Moreover, the observed global orbital motions are well predicted from conservation of point vortex energy and angular momentum.

Departures from the predictions of the point vortex model occur when the separation between vortices is less than 1.6 times their diameter and merger is observed to occur;[9,14] and when the vortices ''scrape'' the cylindrical wall and circulation (charge) is lost. Also, the axial confinement fields cause a dynamically unimportant shift in the orbit frequencies compared to point vortex theory,[16] as has been discussed in Sec. III B 1.

Figure 3 is a typical $n(r, \theta)$ contour map of the electron density of the two vortices, showing bell-shaped profiles extending over a radius $R_v \approx 0.5$ cm, with central density $n(R=0) \approx 3 \times 10^6$ cm^{-3}. The cylinder axis is marked by a small ''x'' symbol; the total center of mass is marked by a larger ''x.'' We characterize the positions of the two identical, spatially extended vortices by the coordinates (r_1, θ_1), (r_2, θ_2) of the two centers-of-mass. From contour plots at various times we obtain motions of the centers of mass.

We observe equilibria in which the two vortices steadily orbit about the center of the cylinder, with either $r_1 = r_2$ or $r_1 \neq r_2$ but always with $\theta_2 = \theta_1 + \pi$. In these equilibria, each vortex orbits at a constant radius and with the same frequency f_{orb}, so the two vortices remain diametrically opposed. For $r_1 = r_2$, both stable and unstable equilibria are observed. That is, if the vortices are initially displaced from the equilibrium positions, they either oscillate around the equilibrium points with frequency f_{osc}, or diverge from the equilibrium points with an exponential rate γ.

In Fig. 4, the measured orbit radii of the stable equilibria are plotted as circles, and the orbit radii of the unstable equilibria as diamonds. No equilibria are observed for $r_1 = r_2 < 0.22$, since the vortices merge together for $(r_1 + r_2)/2r_v \lesssim 1.6$. For larger separations, the $r_1 = r_2$ equilibria are observed to be stable for radii $r < r_H = 0.462$ and unstable for $r > r_H$. All $r_1 \neq r_2$ equilibria are observed to be stable; in Fig. 4, these equilibria are shown as circles, with the arbitrary convention of $r_1 > r_2$.

Figure 5 shows three examples of observed center-of-vorticity positions, relative to a frame rotating about the axis. The three classes of equilibria, two stable and one unstable, are each represented. The two vortices were injected with small initial displacements from equilibrium points. The vortex positions subsequently measured are indicated with square and plus symbols, and the directions (i.e., time ordering) of the oscillations about, or exponentiation away from, equilibrium points are indicated with arrows. The solid lines show fits[9] to the oscillations or exponentiation predicted by point vortex theory, discussed below. As predicted by Havelock, the orbits are unstable for $r > r_H$.

In Fig. 6, we plot the observed rates of oscillation about
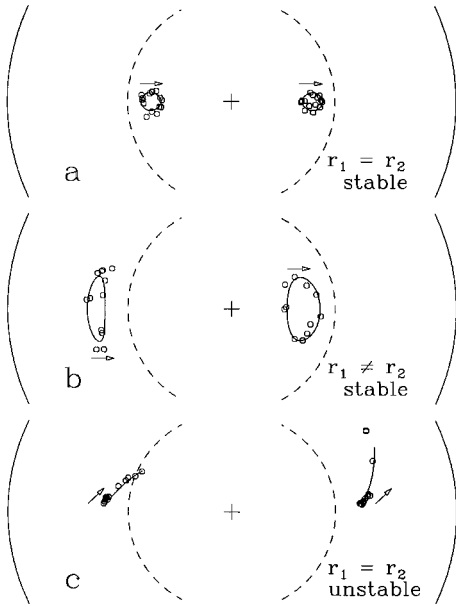
T. B. Mitchell and C. F. Driscoll

FIG. 5. Observed center-of-vorticity positions, in a rotating frame, of vortices orbiting about three classes of equilibria. The arrows show the directions of motions, and the dashed line is $r_H = 0.462$.

stable equilibria, f_{osc}, and the observed exponentiation rate from unstable equilibria, γ. These rates, measured in the rotating frame of the orbit, are normalized by the infinite length orbit frequency f_{orb}^∞, defined below [Eq. (14)]. For $r_1 = r_2$, f_{osc} varies from approximately f_{orb}^∞ down to zero as r_1 is increased from 0.23 to 0.46. For small r, f_{osc} is approximately f_{orb}^∞ because the vortices orbit about the center of (total) mass, independent of where this center is relative to the cylindrical wall. As r approaches 0.46, f_{osc} approaches zero, since the restoring forces go to zero as the influence of the image charges in the wall becomes important. For
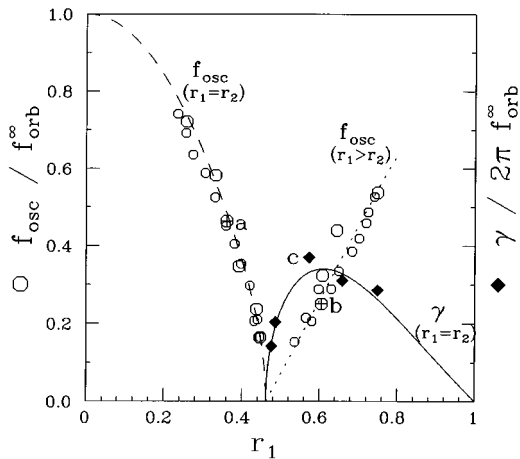

FIG. 6. Normalized measured oscillation frequencies f_{osc} (O) and exponential growth rates γ (diamond). The curves show predictions from an analytic point vortex model, where the solid lines indicate exponential growth and the dashed and dotted lines are oscillation frequencies. The motions corresponding to the three marked rates a,b,c are shown in Fig. 5.

$r_1 = r_2 > 0.46$, initial displacements $\Delta \mathbf{x} \equiv (\Delta r, r \Delta \theta)$ from an equilibrium point are observed to grow exponentially as

$$\Delta \mathbf{x} = A \mathbf{x}_+ \exp(\gamma t) + B \mathbf{x}_- \exp(-\gamma t), \tag{13}$$

where $\mathbf{x}_+$ ($\mathbf{x}_-$) is the growing (decaying) eigenvector. Over the accessible range of unstable equilibria, we observe growth rates $\gamma / 2 \pi f_{orb}^\infty \approx 0.2$ to 0.4, as shown by the diamonds in Fig. 6.

The observed motion of these spatially extended vortices is well-described by point vortex theory. This approximation neglects the effects of surface waves and shape distortions, since the fields outside an extended vortex are the same as the fields outside a point vortex only if the extended vortex is circular. In this approximation, we first consider our 3D confined columns as 2D extended vortices of z-averaged density $n(r, \theta, t)$. We characterize the strength of the extended vortices by their line density $N_L \approx 2 \times 10^6$ cm^{-1}, and then treat the two extended patches as 2 point vortices of circulation $\Gamma \equiv (2 \pi c e / B_z) 2 N_L \approx 10^6$ cm^2 s^{-1} at the centers of mass.

A point vortex generates an azimuthal velocity field with a magnitude inversely proportional to the distance D from the vortex:[25] $|\mathbf{v}| = \Gamma / 2 \pi D$. For an equilibrium characterized by $(r_1, r_2, \theta_2 = \theta_1 + \pi)$, therefore, point vortex 1 is predicted to orbit about the cylinder axis at a frequency

$$f_{orb}^\infty(r_1, r_2) = \frac{\Gamma}{2\pi} \frac{1}{2\pi r_1} \frac{1}{R_w^2} \left[\frac{1}{r_1 + r_2} - \frac{1}{r_1 + 1/r_2} \right.$$
$$\left. + \frac{1}{r_1 - 1/r_1} \right]. \tag{14}$$

The three terms in brackets are the inverse distances from vortex 1 to vortex 2, image 2, and image 1, respectively. The orbit frequency of vortex 2 is given by interchanging the subscripts 1 and 2, so the equilibrium positions are given by the solutions to $f_{orb}^\infty(r_1, r_2) = f_{orb}^\infty(r_2, r_1)$. In addition to the symmetric solution with $r_1 = r_2$, asymmetric solutions exist with $r_1 > r_H > r_2$, as shown by the dotted curve in Fig. 4.

The stability of circular orbits of two or more point vortices within a circular boundary was first analyzed by Havelock.[24] This linear stability analysis predicts oscillation frequencies f_{osc} around stable equilibria with $r_1 = r_2 < r_H \equiv 0.462$ and predicts exponentiation rates $\pm \gamma$ for unstable equilibria with $r_1 = r_2 > r_H$, as shown by the dashed and solid curves in Fig. 6. We have extended the linear stability analysis[9] to equilibria with $r_1 \neq r_2$, and find oscillation frequencies as shown by the dotted curve in Fig. 6. Experimentally, both the stable and unstable dynamics of the 3D electron columns are well-described by the 2D point vortex approximation.

Interestingly, the fully nonlinear motion of 2 point vortices within a cylindrical boundary can be understood from phase space maps, since the system is integrable. There are 4 variables and 2 constants of the motion, the angular momentum per unit length P_θ^{pv}, and the interaction energy per unit length H^{pv}.[25,26] These are written in scaled variables $\bar{P}_\theta$ and $\bar{H}$ as

$$\bar{P} \equiv \frac{P_\theta^{pv}}{P_0} = \sum_{i=1,2} (1 - r_i^2) \tag{15}$$

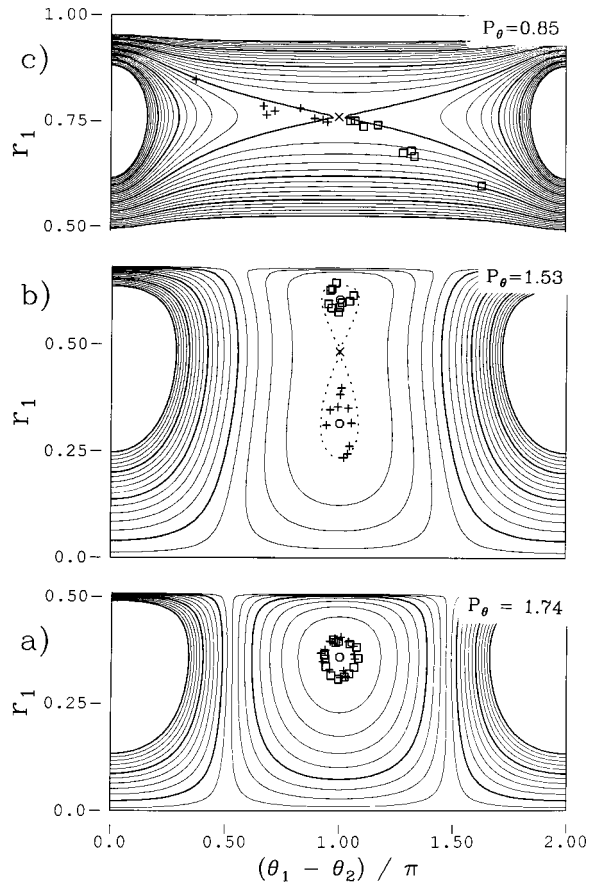T. B. Mitchell and C. F. Driscoll   1833

FIG. 7. Energy contours in configuration space for three values of scaled angular momentum $\bar{P}_\theta$. Minima (O) and saddle points (X) are shown, as are the measured center-of-mass positions of two vortices (square and plus) at a sequence of times. The energy difference between contours is $\Delta H = 0.05$ except in b, where an additional energy contour (dots) at the value of the saddle point is included.

and

$$\bar{H} \equiv \frac{H^{\text{pv}}}{H_0} = \sum_{i=1,2} \ln(1 - r_i^2) + \ln\left[1 + \frac{(1-r_1^2)(1-r_2^2)}{d_{12}^2}\right]. \tag{16}$$

Here, $P_0 \equiv (eB/2c)R_w^2 N_L$ is the angular momentum of an on-axis line charge, and we choose $\bar{P}_\theta = 0$ at $r = r_w = 1$. $H_0 \equiv e^2 N_L^2$ is a characteristic energy, and d_{12} is the normalized separation between the two vortices:

$$d_{12}^2 \equiv |\mathbf{r_1} - \mathbf{r_2}|^2 = r_1^2 + r_2^2 - 2r_1 r_2 \cos(\theta_1 - \theta_2). \tag{17}$$

The motion of the point vortices can be visualized from contour maps of $\bar{H}(r_1, \theta_1 - \theta_2, P_\theta)$. For any given $\bar{P}_\theta$, the vortices move along a contour of constant $\bar{H}$. Given r_1, the second vortex must be at $r_2^2 = 2 - r_1^2 - \bar{P}_\theta$.

There are three distinct map topologies over the accessible range of $0 < \bar{P}_\theta < 2$, and examples of these are shown in Fig. 7. For $\bar{P}_\theta > 2(1 - r_H^2) = 1.57$, there is a minimum energy stable equilibrium (an O-point) with the two vortices symmetrically opposite each other, i.e., $\theta_1 - \theta_2 = \pi$ and $r_1 = r_2$, as shown in Fig. 7(a). For $1 < \bar{P}_\theta < 2(1 - r_H^2)$, the symmetric equilibrium is an unstable saddle point (an X-point), and two

new O-points exist at $r_1 \neq r_2$ values [Fig. 7(b)]. As $\bar{P}_\theta$ decreases, these O-points move further from the X-point. For $\bar{P}_\theta < 1.0$ the O-points disappear, and there are no stable equilibria [Fig. 7(c)].

Also shown by the square and plus symbols in Fig. 7 are the measured center-of-mass coordinates of two vortices, for evolutions with the corresponding $\bar{P}_\theta$. In Fig. 7(a), the center-of-mass of each vortex is observed to oscillate once around the stable equilibrium while the vortices orbit 2.7 times around the center of the trap. The uncertainty in the measured positions corresponds to an uncertainty in energy of $\delta\bar{H} \leq 0.01$, i.e., 1/5 of a contour level. In Fig. 7(b), 3/4 of an oscillation about an asymmetric stable equilibrium is observed, with a larger measurement error corresponding to $\delta\bar{H} \equiv 0.02$ due to additional uncertainties introduced while creating the $r_1 \neq r_2$ equilibria. In Fig. 7(c), the vortices exponentiate away from the unstable equilibrium, with the displacements being largely in the $\hat{\theta}$-direction. The large measurement errors at long times reflect the difficulty in repeatably following the exponentially unstable trajectories.

Spatially extended (non-point) vortices may change shape, and the energy of the system may vary from that given by Eq. (16) when the vortices deviate from circularity. Experimentally, we observe elongations away from circularity of $\leq 10\%$ in general, and up to 30% for $r_1 = r_2 \sim 0.2$ (near merger). These time-varying eccentricities have not, however, been observed to cause experimentally noticeable departures from the predictions of the point vortex model. This result is perhaps because the energies involved in elongation are relatively small: using a moment model,[16] we estimate $\delta\bar{H} \sim 0.002$ and 0.02 for elongations of 10% and 30%, respectively.

The double vortex state can be manipulated by external control of the overall energy and angular momentum of the system. Previous work on the dynamics of a single vortex has established that resistive destabilization[27] and active feedback,[28] which change P_θ and H, cause the observed motions to evolve accordingly. We have found similar effects for the 2 vortex state.

For example, a resistance between azimuthal sections of the wall will dissipate the energy, and lower the angular momentum, of the system. If a resistance is switched on when two vortices are near stable equilibrium points, the vortices will remain near stable equilibria while the equilibrium orbit radii increase with time. During an evolution with initial vortex positions of $r_1 = r_2 \approx 0.3$, the radii were observed to increase to $r_1 = r_2 = r_H$, after which r_1 increased until vortex 1 was pressed against the wall, while r_2 had decreased to $r_2 \approx 0.1$. This technique was occasionally used in the investigation of 2 vortex dynamics to shift the vortices from one stable equilibrium to another.

In Sec. VI, we describe merger experiments on vortices with equal peak vorticity, but different radii. We note here that the orbital dynamics of these asymmetric vortices was also compared with the predictions of point vortex theory, and close agreement with point vortex theory was observed.
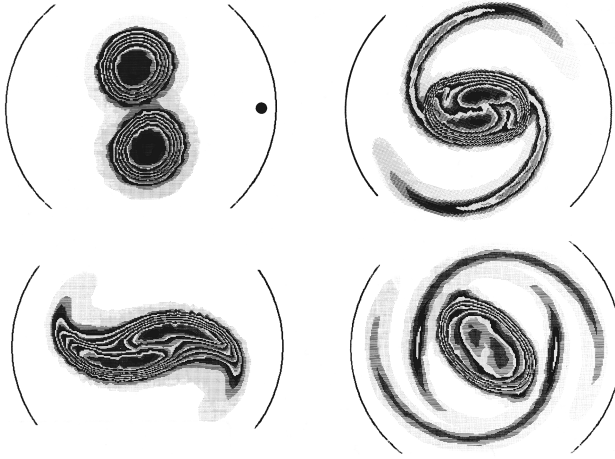
FIG. 8. $n(r,\theta,t)$ density (vorticity) plots of two symmetric vortices unstable to merger, at times 0, 16, 41 and 76 μs. The density between solid contours is 2.9×10^5 cm^{-3}. Here, the vortices have radii $r_{v2}=r_{v1}=0.25$ and radial positions $r_2=r_1=0.30$.
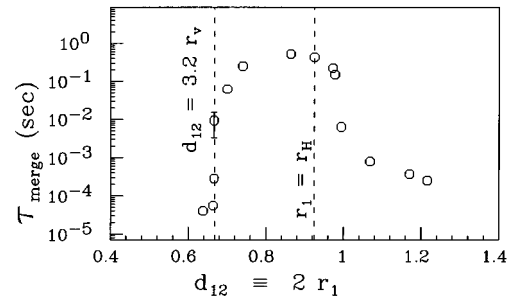

FIG. 9. Merger time versus separation for two vortices with radii $r_v=0.21$ injected at diametrically opposite positions $r_1=r_2$, showing merger instability and orbit instability.

V. SYMMETRIC VORTEX MERGER MEASUREMENTS

Merger is a fundamental vortex property. When two like-signed spatially extended vortices approach close enough, they are susceptible to a pairing instability which causes them to wrap into a single larger core, accompanied by the ejection of filaments. Prior work has used analytic theory, moment models and numerical simulations to investigate merger.[16,29–31] These have established that for sufficiently large vortex separation, elongated vortex equilibria exist with the two vortices orbiting about each other. As the separation between the vortices is decreased, the elongation becomes more pronounced until ultimately a separation is reached where there is no stable equilibrium. At this point, the two vortices drift towards and wrap around each other, ejecting narrow filaments of vorticity in the process. Merger of inviscid vortices is, in theory, predicted to conserve the energy, angular momentum, and all moments of the density. The enstrophy Z_2, is the second moment, given by

$$Z_2 \equiv \frac{\int dr \int r \, d\theta n^2(r,\theta)}{[\int dr \int r \, d\theta n(r,\theta)]^2}. \tag{18}$$

Figure 8 is a series of density plots showing the merger of two electron vortices initially placed close together. From such time sequences, we observe the evolution of the total electron number, angular momentum, electrostatic energy, and enstrophy. During merger, the total density, angular momentum, and energy are all conserved within the scatter ($\pm 1\%$) of the experimental measurements. The enstrophy, however, decreases to 82% of its initial value. Some, but likely not all,[32] of this decrease is due to the ''coarse-graining'' of the increasingly fine spatial scales by the collimator hole. The relative size of the collimator is indicated by the solid dot in Fig. 8; its size sets the minimum spatial scales resolved.

Two simulations of vortex merger, with very similar initial conditions to those of Fig. 8, have been published in the literature. They are Fig. 1 of Melander et al.[16] from a high-

resolution direct numerical simulation, and Fig. 1 of Waugh,[33] from a contour dynamics simulation with 8 contour levels. Both of these simulations closely resemble Fig. 8.

While vortex pairing has been often observed in conventional fluids experiments, with perhaps the first clear evidence for it from Freymuth,[3] viscous and boundary effects have usually resulted in non-ideal behavior being observed. One example of this is the experiments of Cardoso, Marteau and Tabeling,[34] who used thin layers of electrolyte to study decaying quasi-2D turbulent flows and found strong dissipation of energy and peak vorticity. Another example is the rotating water tank experiment of Griffiths and Hopfinger,[35] where for one sign of vorticity merger was observed to occur for all initial separations. In contrast, merger experiments with electron vortices typically show close agreement with the predictions of near-inviscid theory.

In these bounded systems, vortex merger can occur either because the vortices are initially close together, or because the orbits are unstable in the point vortex sense. The first electron vortex merger experiments studied the onset of merger for electron vortices injected onto Havelock-stable (i.e., $r_1=r_2<0.46$ and $\theta_2-\theta_1=\pi$) equilibrium points.[24] The time until merger, τ_{merge}, versus vortex separation shows an abrupt increase at $r_1=0.33=1.6r_v$, as seen in Fig. 9. The electron vortices merge immediately for initial separations $d_{12}\equiv 2r_1=0.64=3.1r_v$, and orbit for more than 10^4 orbits for separations $d_{12}>3.4r_v$. This result is in good agreement with theory, which has predicted critical separations for this instability in the range of 2.86 to 3.4 vortex radii.[30,36] It has also been established that the vortex size is the relevant length scale for separation, since the merger curves for vortices with different radii overlay each other when the separation between them was scaled by their radius.[11]

Figure 9 also shows that as r_1 is increased past r_H, the lifetime begins to drop sharply. This decrease in lifetime is believed to be due to enhanced column expansion from ''orbital pumping.'' The columns are increasing in radius during thousands of orbits, and merger occurs when the radii finally become large enough to satisfy the merger criterion of $r_v \gtrsim d_{12}/3.2$. This orbital pumping expansion occurs because the vortices are injected onto unstable equilibrium points, and their subsequent motion includes large radial excursions away from their initial points as the vortices orbit about the
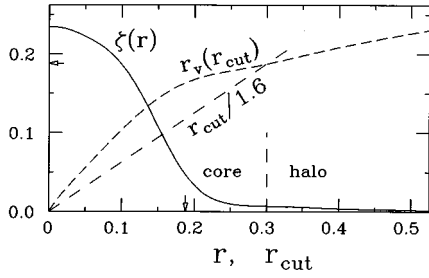
FIG. 10. Vorticity profile $\zeta(r)$ and $r_v(r_{cut})$ from Eq. (19). The core/halo boundary occurs at $r_{cut}=0.3$, where $r_{cut}/1.6=r_v(r_{cut})$.
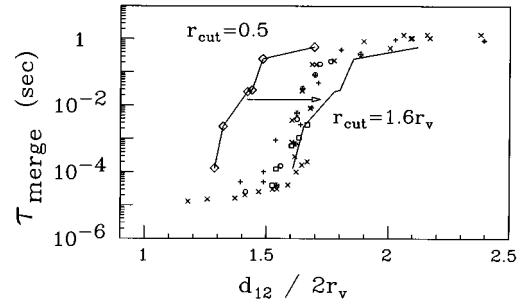

FIG. 11. Measured merger time versus separation for vortices with the haloed profile of Fig. 10. The diamonds are the separations scaled to $r_v=0.23$ with $r_{cut}=0.5$. Use of $r_{cut}=1.6r_v$ gives a smaller vortex radius which shifts the merger curve, as indicated by the arrow. All other data points are for sharp-edged profiles.

stable points. The radial excursions cause variations in the axial length of the vortices, and these excursions are dissipated by compressional (or "second") viscosity.[21] Finally, at the very largest separations shown, lifetimes become extremely short (several orbits) because the trajectories of the vortices after injection cause them to essentially drift into each other, and merge.

Here, the vortex radius is calculated from the 2D distribution by

$$r_v \equiv \frac{3}{2}\frac{1}{N_L}\int_0^{r_{cut}} dA\, r'\, \zeta(r,\theta), \qquad (19)$$

where the (r,θ) integral is over the area of the vortex and $r' \equiv |\mathbf{r}-\mathbf{r}_{cm}|$ is centered on the center-of-vorticity of the vortex. This is simply a density-weighted radial integral from the center of the vortex, ending at r_{cut}, defined to be the vortex edge. This integral was found to accurately characterize the effective radius with respect to merger for a range of vorticity profiles.[11] The factor of 3/2 is included to ensure that a top hat profile with radius R has $R_v=R$. With the sharp-edged profiles of the prior experiment, the cut-off at r_{cut} is naturally taken to be the point where the density goes to zero.

For less sharp vorticity profiles, the calculation of R_v from Eq. (19) depends on the cut-off radius r_{cut} beyond which vorticity is not part of the given vortex. We take $r_{cut}=1.6r_v$, and find this to be a workable and self-consistent definition. Essentially this says that vorticity past r_{cut} could be advected away or captured by a second vortex even if the second vortex were not within $1.6r_v$ as required for merger.

Figure 10 illustrates the self-consistency of the definition $r_{cut}=1.6r_v$ (r_{cut}). The vorticity profile $\zeta(r)$ is that resulting from the merger of 2 symmetric vortices, and has an extended halo. The integral $r_v(r_{cut})$ increases from zero as r_{cut} increases from zero, initially with unity slope. The point where $r_v(r_{cut})=r_{cut}/1.6$, marked by the dashes at $r_{cut}=0.30$, defines the end of the vortex core and the beginning of the halo. It gives $r_v=0.188$, as shown by the arrows.

As a test of the vortex radius definition, we have measured τ_{merge} versus separation for two haloed vortices with the profile of Fig. 10. This profile has a radius of $r_v=0.188$ for $r_{cut}=1.6r_v=0.30$, and would have a radius of $r_v=0.23$ for $r_{cut}=0.5$. In Fig. 11 we plot the measured merger times versus separation d_{12} scaled by both of these values of r_v. In addition, we include data from merger of

sharp-edged profiles.[11] It can be seen that the vortex radius algorithm leads to an accurate prediction of when a haloed vortex will be susceptible to the pairing instability, as the merger curve overlays the other data for short τ_{merge} values when the cut-off $r_{cut}=1.6r_v$ is imposed.

VI. ASYMMETRIC VORTEX MERGER MEASUREMENTS

In this section we describe merger experiments with two vortices which have different radii but equal central vorticity, to obtain insight into more complicated systems of many interacting vortices. The peak vorticity of the final merged core is observed to be roughly the same as that of the merging vortices. The fraction of the total circulation entrained into the central core varies from 70% to 90% as the initial vortex radii are varied from 1:1 to 2:1. This fraction, as well as the time required to merge, τ_{merge}, depends on the initial placement of the two vortices. We also find that the self-energy of the central core is roughly equal to the sum of the self-energies of the merging vortices. These results are in reasonable agreement with the premises of the punctuated Hamiltonian models.

In Fig. 12 we show four $n(r,\theta)$ plots of the merger of two vortices asymmetric in radius but with the same peak vorticity ζ_{peak}. The initial injection points are well away from equilibrium positions, and the ratio of radii is 2:1. The final plot has small points which indicate where the collimator hole (with size shown by the solid dot) was centered; the $n(r,\theta)$ plots are generated by interpolation between the data grid. The smaller vortex is observed to be strained out into a filament. The observed filament width is the result of convolution, by the collimator hole, of a substantially narrower filament. Although the actual structure of the filament is not resolved, when deconvolution is done on the 2D plots, it is found that the data is consistent with filaments having near-zero width. These plots appear qualitatively similar to those of Fig. 7 of McWilliams,[4] which shows a numerical simulation of an asymmetric merger event where the ζ_{peak} of the two vortices is not the same. Here, we also measure the final merged vortex profile at late times.

Our data set for quantifying asymmetric merger consist of many plots like Fig. 12, as well as information from wall
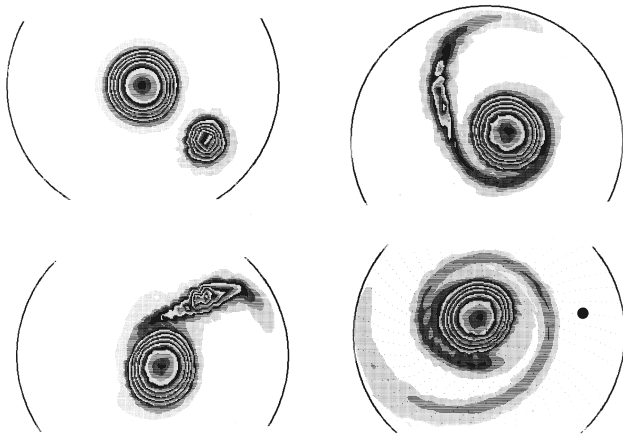
FIG. 12. Density plots of two asymmetric vortices merging, at times 0, 15, 30 and 60 μs. Density between solid contours: 4.9×10^5 cm^{-3}. The positions where the data have been taken, and the collimator hole size, are indicated on the final plot. Here $r_{v2} = 0.50 r_{v1} = 0.13$, $r_1 = 0$ and $r_2 = 0.62$.
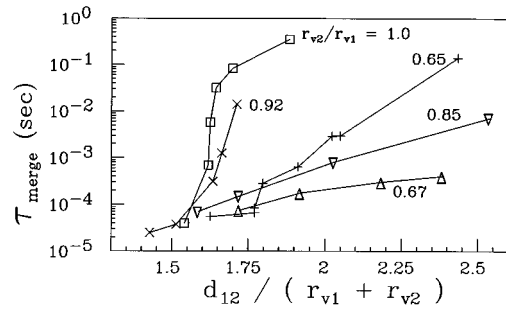

FIG. 13. Asymmetric vortex merger times versus separation, with d_{12} normalized to $(r_{v1} + r_{v2})$. The radius ratio r_{v2}/r_{v1} is indicated for each curve.

probe signals on when merger took place. The profile and peak vorticity of the initial vortices was kept as constant as possible, while the radii and initial separation were varied. Note that this also varied the positions of the equilibrium points, given by $\Gamma_1 r_1 \approx \Gamma_2 r_2$ from Eq. (14). Some initial conditions had the vortices at the equilibrium points, whereas some had $r_1 = 0$, as tabulated in Table I. The initial conditions are indicated by symbols used in later plots.

A. Merger times

Figure 13 shows τ_{merge} versus separation d_{12} for the five different initial conditions of Table I. In the figure, d_{12} has been scaled by the sum of the radii of the two vortices. As was seen in the symmetric merger case, the initial separation of the vortices has an important impact on τ_{merge}. Additionally, vortices injected onto stable equilibrium positions have significantly longer lifetimes than those injected onto unstable equilibrium positions. Two of the initial conditions have the same radius asymmetry of $r_{v2}/r_{v1} \sim 0.66$, but differ in the initial placement, permitting this effect to be isolated. As previously discussed, orbital pumping of compressional viscosity[21] is believed responsible for the observed differences in lifetime.

In two papers on the punctuated Hamiltonian model, the critical separation d_c for immediate merger has been taken to be $d_c = 1.7(r_{v1} + r_{v2})$ by Benzi *et al.*[6] and $d_c = 1.65(r_{v1} + r_{v2})$ by Carnevale *et al.*[5] A more recent paper by Weiss and McWilliams[7] has used an elliptical moment

model to determine the critical separation d_c for merger, and found a good fit to the results of the numerical integrations with

$$\frac{d_c}{r_{v1} + r_{v2}} = 1.6\left(1 + \frac{r_{v1} - r_{v2}}{r_{v1} + r_{v2}}\right). \tag{20}$$

Experimentally, we consider the critical distance to be that which results in merger in about 1 orbit. In Fig. 14 we plot the measured separations, as a function of relative radii, which bracket the critical distance. The smaller distances (at each r_{v2}/r_{v1} value) resulted in merger in less than one orbit period, while the larger distances resulted in at least one orbit before merger. The merger predictions of Weiss and McWilliams,[7] Carnevale *et al.*[5] and Benzi *et al.*[6] are also shown. The data, while not fully conclusive, supports the predictions of Eq. (20).

B. Completeness of asymmetric merger

The question of whether there are significant differences between merger of symmetric vortices and merger of vortices asymmetric in radius is an important and controversial one. The picture of asymmetric merger expected from the symmetric studies was that either two vortices would stably orbit about each other (elastic interaction) or merge, forming a merged core larger than either vortex (complete merger). However, Dritschel and Waugh[8] have used contour dynamics simulations of two isolated top hat profile vortices to investigate this, and found that many unexpected interactions were seen. Specifically, they found that for some separations,
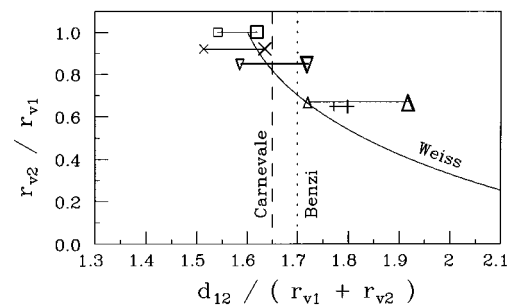
TABLE I. Initial conditions for the data of Figs. 13–15.

r_{v2}/r_{v1}	r_{v1}	Initial placement	Symbol
1.0	0.147	$r_1 = r_2$	□
0.92	0.188	$\Gamma_1 r_1 \approx \Gamma_2 r_2$	x
0.65	0.228	$\Gamma_1 r_1 \approx \Gamma_2 r_2$	+
0.85	0.176	$r_1 = 0$	▽
0.67	0.181	$r_1 = 0$	△
0.54	0.237	$r_1 = 0$	0

FIG. 14. Separations d_{12} giving merger in less than 1 orbit period (small symbols) and in more than an orbit period (large symbols), for various radius ratios r_{v2}/r_{v1}. Various merger criteria are also shown.
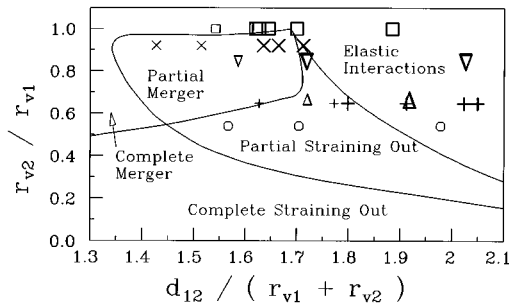
FIG. 15. Asymmetric vortex merger data showing complete merger in less than 1 orbit (small symbols) and in more than 1 orbit (larger symbols). Regions characterizing the contour dynamics simulations of Dritschel and Waugh are also shown.

partial mergers took place where vorticity would be exchanged, but both vortices would survive and elastically interact after the partial merger event. They also found that there could be both partial and complete straining out events, where the vorticity ejected by the smaller vortex does not become associated with the larger vortex. They thus found that smaller vortices were often produced by asymmetric merger, and concluded that it is misleading to expect simple merger of unequal vortices.

In contrast, the confined asymmetric electron vortices typically exhibit simple merger: We find little evidence for partial merger events resulting in two altered and stable vortices. The density plots can follow merger for several orbit periods before they become too noisy to be useful, and these always show merging vortices to join, and any filaments to rapidly become strained and reduced in ζ_{peak}. Occasionally, small coherent patches of vorticity become ejected: An example of this in symmetric merger can be seen in Fig. 8(d), where the filaments show maxima. These maxima, however, are observed not to persist as the filaments wind about the merged core.

If persistent vortex cores were common stable structures of the post-merger electron plasma system, one would expect to detect them on the non-phase-locked radial profiles, where they would show up as higher values of density seen intermittently in the halo. Such anomalously higher values have not been seen, either in the many profiles taken to characterize the final state of merger (i.e., after ~ 20 ms), or profiles taken just after merger specifically to look for this effect. One would also expect the presence of persistent cores after a partial merger to show up on the sector probe signals. What is actually seen is the complicated 2 vortex orbital signature, followed by a single orbital frequency after merger. The transition between the orbit waveform and the single frequency waveform occurs in about one orbit period, and the waveform after merger only rarely shows frequencies in addition to the single orbital frequency.

For perspective, we compare our results to those of Dritschel and Waugh[8] in Fig. 15. Here the data of Fig. 14 is plotted with the ordinate indicating relative radii r_{v2}/r_{v1}. The small symbols indicate complete merger observed within 1 orbit period, and the larger symbols indicate complete merger in more than 1 orbit. The labelled regions are

from Fig. 5 of Ref. 7, transformed to our variables, and indicate the results from contour dynamics simulations. Many of the experimental points are in regions where partial merger or partial straining out is predicted, yet only complete mergers were observed with the confined electron vortices.

Several effects make the electron vortex dynamics significantly different from the contour dynamics simulations. First, the electron dynamics is significantly affected by inviscid symmetrization of vortices by beat-wave damping,[37] which tends to prevent extreme distortions and filamentation. This effect has recently been observed in contour dynamics simulations with 11 contour levels;[38] presumably it requires contour spacings close enough to represent the trapped fluid resonance. Similar inviscid damping would be expected in other fluid systems such as atmospheric flows, protostellar and galactic disks,[39] or drift waves in rotating plasmas.[40] Second, the vortices never separate from each other: The largest merger times in Fig. 13 represent over 10^4 orbits, and the characteristics of these 2 vortex orbits are influenced by the cylindrical boundary. Finally, the dynamics after hundreds of orbit times may be affected by 3D diffusion or dissipative effects such as compressional viscosity and orbital pumping, which are specific to electron plasmas.

These experiments and recent computer simulations[38,41] suggest that even small viscous dissipation can significantly affect vortex interactions. In the simulations, comparisons are made between pseudospectral simulations with normal and hyper viscosity and contour surgery simulations with essentially no viscosity. Particularly relevant is Ref. 38, treating asymmetric merger in the ''partial straining out'' regime of Dritschel and Waugh.[8] The smaller vortex persisted in the contour surgery simulations, but always merged into the larger one in the normal viscosity simulations; this ultimately produced a central core surrounded by a lower density halo, as observed in the electron vortex experiments.

Several effects contribute to diffusion and dissipation in the electron vortex system. Most significant is the dissipation and transport arising from compressional viscosity acting on axial length changes; here, the (r, θ) flows cause axial compressions or elongations[21,22] due to the (r, z) curvature of the end confinement potentials.[19] A single off-axis vortex thus slowly increases in diameter and moves back towards the trap axis due to ''rotational pumping.''[22] Similarly, this effect causes two vortices to slowly increase in diameter (and subtly alters their orbits) due to ''orbital pumping.'' Vortex lifetimes greater than 0.1 s (10^4 orbits) in Fig. 13 are definitely affected by compressional viscosity.

Surprisingly, viscosity acting directly on shears in the (r, θ) flows[42] is typically negligible on the time scales considered here, even when non-local plasma effects[43] are included. Similarly, diffusive effects due to ''anomalous transport'' from construction asymmetries in the magnetic field or in the cylindrical wall occur on much longer time scales at the high fields used here.[20]

In comparison to Navier Stokes simulations with normal viscosity, however, the total dissipation in the electron system is quite low. For example, Yao and Zabusky[38] find that the electron system dissipates surface waves less rapidly than their least dissipative run, which had $\nu_2 = 1.28 \times 10^4$. We
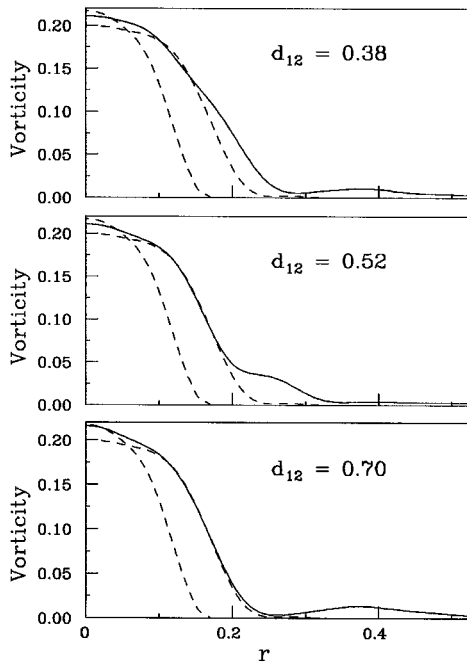
T. B. Mitchell and C. F. Driscoll

FIG. 16. Radial profiles after merger (lines), and for the large and small vortices before merger (dashed). The radius ratio was $r_{v2}/r_{v1}=0.67$, and the initial separation d_{12} is indicated.

must emphasize, however, that the plasma evolution equation including viscosity is *not* the Navier Stokes equation, so no simple comparison between plasma and fluid viscous effects can be made. Two fundamental differences from fluid viscosity are that plasma viscosity gives rise to compressibility in the otherwise incompressible (r,θ) flow, and the plasma viscosity is necessarily proportional to the vorticity (i.e., the electron density).

C. Conserved quantities: core and halo

The images of vorticity taken during asymmetric vortex merger, such as Figs. 8 and 12, show that the detailed evolution sensitively depends on the initial conditions, but always results in a central core surrounded by filaments winding about it. This distribution then axisymmetrizes, on a timescale of tens to hundreds of rotations (several milliseconds), into a core surrounded by a halo.

In order to quantify the evolution of the system during merger, for each initial condition detailed in Table I we have taken radial profiles of the vortices both before and ~ 20 msec after the merger. This particular time after merger was selected because it is long (~ 1000 self-rotations) on the time scale of filament windings about the core, but short on the time scale of plasma confinement.

The final state vorticity profile depends on the sizes and separations of the two vortices. In Fig. 16 we show the radial profiles resulting from merger with $r_{v2}/r_{v1}=0.67$ and three different initial separations. The initial radial profiles of the 2 vortices before merger are also shown by the dashed lines. One can readily see the effect of the initial separation: The smaller d_{12} is, the more compact the merged profile.
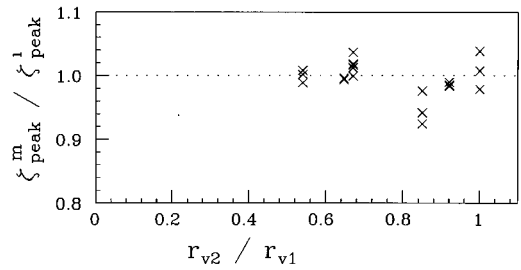

FIG. 17. Ratio of peak vorticity of merged and initial profiles.

In Fig. 17 we plot the ratio of the measured ζ_{peak}^{m} after merger to its value ζ_{peak}^{i} before merger. Before merger, the two vortices had the same ζ_{peak}. While there is a fair amount of scatter, ζ_{peak} appears to be conserved during merger, as the average of the measured ratio is 0.994 ± 0.026. This result is in agreement with simulations, at least for asymmetric merger. In a merger study, Melander *et al.*[31] found that for asymmetric merger the larger vortex becomes the central region of the core, resulting in its original ζ_{peak} being the final ζ_{peak} of the core.

For the final merged core, we designate the circulation within $r=1.6r_v$ by Γ_{core}^{m}, and the total circulation by Γ_{tot}^{m}. In Fig. 18 we plot the ratio of the measured circulations after merger with the values Γ_1 and Γ_2 before merger. The data marked by (X) indicate $\Gamma_{\text{tot}}^{m}/(\Gamma_1+\Gamma_2)$, and are thus expected to be equal to 1, since total circulation (charge) is well conserved in this system. The variations in Γ_{tot}^{m} reflect the accuracy of the radial integrals of the measured profiles. The average of the data is $\Gamma_{\text{tot}}^{m}/(\Gamma_1+\Gamma_2)=1.00\pm0.02$.

The data marked by circles is $\Gamma_{\text{core}}^{m}/(\Gamma_1+\Gamma_2)$, and thus indicate the fraction of the initial circulation bound in the core after merger. We find that between 70% and 90% of the circulation remains bound in the core after merger, with some indication that this percentage increases as r_{v2}/r_{v1} decreases. The variation at each r_{v2}/r_{v1} value is systematic, and depends on the initial separation of the vortices in the manner one would expect from Fig. 16: The greater the initial separation, the more extended the merged profile and the
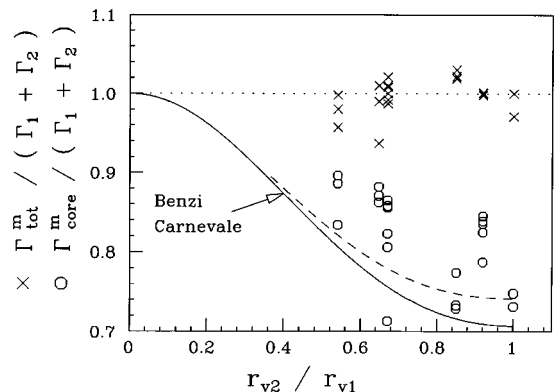

FIG. 18. Core and total circulations of the merged state, normalized to total initial circulation, versus r_{v1}/r_{v2}. Line is prediction for top hat profile vortices, and dashed line includes effect of circular boundary.

Phys. Fluids, Vol. 8, No. 7, July 1996

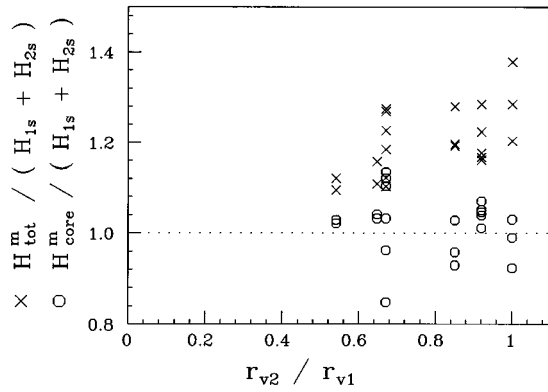T. B. Mitchell and C. F. Driscoll   1839

FIG. 19. Core and total energies after merger, normalized to the total initial self-energy, versus r_{v2}/r_{v1}.

less circulation from the smaller vortex in the merged core. These results can be compared with the merger rules used by Carnevale et al.[5] and Benzi et al.[6] Using arguments involving conservation of kinetic energy per unit area,[5] or involving enstrophy dissipation,[6] these authors independently came up with a simple merger rule of

$$r_{vm}^4 = r_{v1}^4 + r_{v2}^4. \tag{21}$$

This gives the ratio of circulation bound in the core as $r_{vm}^2/(r_{v1}^2 + r_{v2}^2)$. We plot this prediction (solid line) in Fig. 19, as well as a prediction (dashed line) based on a merger rule of

$$r_{vm}^4\left[\frac{1}{4} - \ln r_{vm}\right] = r_{v1}^4\left[\frac{1}{4} - \ln r_{v1}\right] + r_{v2}^4\left[\frac{1}{4} - \ln r_{v2}\right]. \tag{22}$$

This latter rule takes into account the effect of the wall on the energies of top hat vortices.[9] While the data shows a large amount of scatter, it is apparent that the measured values are systematically somewhat higher than those predicted by the merger rules for top hat vortices, possibly because of the continuous vorticity distribution of the electron vortices.

Merger is observed (and predicted) to conserve the total energy H_ϕ of the system. Before merger, the energy can be conceptually broken into ''self-energies'' of the vortices, H_{1s} and H_{2s}, and terms due to their interaction with each other and with the image charges, H_{int}. After merger, there are no interaction energy terms between vortices, but we can consider both a total electrostatic energy of the final merged system H_{tot}^m, and a core self-energy H_{core}^m where r_{cut} is used to discard the halo. Energy conservation is then $H_{tot}^m = H_{core}^m + H_{halo}^m = H_{1s} + H_{2s} + H_{int}$. Carnevale et al.,[5] in order to derive Eq. (22), used as a conserved quantity the self-energy of the merging vortices, i.e., $H_{1s} + H_{2s} = H_{core}^m$. This is equivalent to asserting that the interaction energy between the merging vortices gets dispersed into the halo. We have compared Carnevale's conjecture with our data, by measuring the self energies of the merging vortices, and of the merged profile with and without using r_{cut} to discard the halo. The energies here were calculated from the 3D quantities for maximum accuracy. We first calculated the self-

consistent 3D potential $\phi(r,\theta,z,t)$ and density $\tilde{n}(r,\theta,z,t)$ distributions from the measured on-axis density profiles,[9] and then used the 3D version of Eq. (7).

In Fig. 19 we plot the quantities $H_{tot}^m/H_{1s} + H_{2s}$ and $H_{core}^m/H_{1s} + H_{2s}$. As in the bound circulation data, the variation at each value is systematic. As expected, the initial interaction energy is missing: Averaging all the points, $H_{tot}^m/H_{1s} + H_{2s} = 1.20 \pm 0.07$. We find, however, that the mean of the $H_{core}^m/H_{1s} + H_{2s}$ points is 1.02 ± 0.07. While this measurement is of course dependent on our particular definition for the core and halo, this result seems to indicate that Carnevale's conjecture is not an unreasonable one.

Returning now to the question of the amount of circulation bound in the halo, we note that the merger rules of Eqs. (21) and (22) were derived from the principle that the self-energy of top hat vortices is conserved during merger. Since self-energy is found experimentally to be roughly conserved, this suggests that the discrepancy seen in Fig. 19, between the measurements and predictions based on these merger rules, might be due to the non-top hat profile of the electron vortices.

ACKNOWLEDGMENTS

[1] R. H. Levy, ''Two new results in cylindrical diocotron theory,'' Phys. Fluids **11**, 920 (1968); R. J. Briggs, J. D. Daugherty, and R. H. Levy, ''Role of Landau damping in crossed-field electron beams and inviscid shear flow,'' ibid. **13**, 421 (1970).

[2] C. F. Driscoll and K. S. Fine, ''Experiments on vortex dynamics in pure electron plasmas,'' Phys. Fluids B **2**, 1359 (1990).

[3] P. Freymuth, ''On the transition in a separated laminar boundary layer,'' J. Fluid Mech. **25**, 683 (1966).

[4] J. C. McWilliams, ''The emergence of isolated coherent vortices in turbulent flow,'' J. Fluid Mech. **146**, 21 (1984).

[5] G. F. Carnevale, J. C. McWilliams, Y. Pomeau, J. B. Weiss, and W. R. Young, ''Evolution of vortex statistics in two-dimensional turbulence,'' Phys. Rev. Lett. **66**, 2735 (1991).

[6] R. Benzi, M. Colella, M. Briscolini, and P. Santangelo, ''A simple point vortex model for two-dimensional decaying turbulence,'' Phys. Fluids A **4**, 1036 (1991).

[7] J. B. Weiss and J. C. McWilliams, ''Temporal scaling behavior of decaying two-dimensional turbulence,'' Phys. Fluids A **5**, 608 (1993).

[8] D. G. Dritschel and D. W. Waugh, ''Quantification of the inelastic interaction of unequal vortices in two-dimensional vortex dynamics,'' Phys. Fluids A **4**, 1737 (1992).

[9] T. B. Mitchell, ''Experiments on electron vortices in a Malmberg-Penning trap,''Ph.D. thesis, University of California, San Diego, 1993.

[10] T. B. Mitchell, C. F. Driscoll, and K. S. Fine, ''Experiments on stability of equilibria of two vortices in a cylindrical trap,'' Phys. Rev. Lett. **71**, 1371 (1993).

[11] K. S. Fine, C. F. Driscoll, J. H. Malmberg, and T. B. Mitchell, ''Measurements of symmetric vortex merger,'' Phys. Rev. Lett. **67**, 588 (1991).

[12] J. H. Malmberg and J. S. deGrassie, ''Properties of a nonneutral plasma,'' Phys. Rev. Lett. **35**, 577 (1975).

[13] F. M. Penning, ''Glow discharge at low pressure between coaxial cylinders in an axial magnetic field,'' Physica **3**, 873 (1936).

[14] R. C. Davidson, Physics of Nonneutral Plasmas (Addison-Wesley, Redwood City, 1990).

[15] G. K. Batchelor, ''Computation of the energy spectrum in homogeneous two-dimensional turbulence,'' Phys. Fluids **12**, 233 (1969).

[16]M. V. Melander, N. J. Zabusky, and J. C. McWilliams, ''Symmetric vortex merger in two dimensions: Causes and conditions,'' J. Fluid Mech. **195**, 303 (1988).

[17]K. S. Fine, ''Experiments with the $l=1$ diocotron mode,'' Ph.D. thesis, University of California, San Diego, 1988.

[18]K. S. Fine, ''Simple model of finite length diocotron mode,'' Bull. Am. Phys. Soc. **36**, 2331 (1991).

[19]A. J. Peurrung and J. Fajans, ''A limitation to the analogy between pure electron plasmas and two-dimensional inviscid fluids,'' Phys. Fluids B **5**, 4295 (1993).

[20]C. F. Driscoll, K. S. Fine, and J. H. Malmberg, ''Reduction of radial losses in a pure electron plasma,'' Phys. Fluids **29**, 2015 (1986).

[21]B. P. Cluggish and C. F. Driscoll, ''Transport and damping from rotational pumping in magnetized electron plasmas,'' Phys. Rev. Lett. **74**, 4213 (1995); B. P. Cluggish and C. F. Driscoll, ''Transport and sawtooth oscillations from rotational pumping of a magnetized electron plasma,'' Phys. Plasmas **3**, 1813 (1986).

[22]S. M. Crooks and T. M. O'Neil, ''Rotational pumping and damping of the $m=1$ diocotron mode,'' Phys. Plasmas **2**, 355 (1994).

[23]A. W. Hyatt, C. F. Driscoll, and J. H. Malmberg, ''Measurement of the anisotropic temperature relaxation rate in a pure electron plasma,'' Phys. Rev. Lett. **59**, 2975 (1987).

[24]T. H. Havelock, ''The stability of motion of rectilinear vortices in ring formation,'' Philos. Mag. **11**, 617 (1931).

[25]H. Aref, ''Chaos in the dynamics of a few vortices—fundamentals and applications,'' in *Theoretical and Applied Mechanics*, Proceedings of the Sixteenth International Congress, Lyngby, Denmark 19–25 August 1984, edited by F. I. Niordson and N. Olhoff (North-Holland, Amsterdam, 1985).

[26]T. M. O'Neil, ''Cooling of a pure electron plasma by cyclotron radiation,'' Phys. Fluids **23**, 725 (1980).

[27]W. D. White, J. H. Malmberg, and C. F. Driscoll, ''Resistive wall destabilization of diocotron waves,'' Phys. Rev. Lett. **49**, 1822 (1982).

[28]W. D. White and J. H. Malmberg, ''Feedback damping of the $l=1$ diocotron wave,'' Bull. Am. Phys. Soc. **27**, 1031 (1982).

[29]K. V. Roberts and J. P. Christiansen, ''Topics of computational fluid mechanics,'' Comput. Phys. Commun. **3**, 14 (1972).

[30]P. G. Saffman and R. Szeto, ''Equilibrium shapes of a pair of equal uniform vortices,'' Phys. Fluids **23**, 12 (1980).

[31]M. V. Melander, N. J. Zabusky, and J. C. McWilliams, ''Asymmetric vortex merger in two dimensions: Which vortex is 'victorious'?'' Phys. Fluids **30**, 2610 (1987).

[32]X.-P. Huang and C. F. Driscoll, ''Relaxation of 2D turbulence to a metaequilibrium near the minimum enstrophy state,'' Phys. Rev. Lett. **72**, 2187 (1994).

[33]D. W. Waugh, ''The efficiency of symmetric vortex merger,'' Phys. Fluids A **4**, 1745 (1992).

[34]O. Cardoso, D. Marteau, and P. Tabeling, ''Quantitative experimental study of the free decay of quasi-two-dimensional turbulence,'' Phys. Rev. E **49**, 454 (1994).

[35]R. W. Griffiths and E. J. Hopfinger, ''Coalescing of geostropic vortices,'' J. Fluid Mech. **178**, 73 (1987).

[36]V. J. Rossow, ''Convective merger of vortex cores in lift generated wakes,'' J. Aircraft **14**, 283 (1977).

[37]T. B. Mitchell and C. F. Driscoll, ''Symmetrization of 2D vortices by beat-wave damping,'' Phys. Rev. Lett. **73**, 2196 (1994).

[38]H. B. Yao and N. J. Zabusky, ''Resonance induced symmetrization of an isolated vortex region,'' submitted to Phys. Fluids.

[39]N. Mattor and T. B. Mitchell, ''Scattering of spiral density waves to lower arm number,'' to appear in Astrophys. J.

[40]T. S. Hahm, ''Flow-shear-induced Compton scattering of electron drift instability,'' Phys. Fluids B **4**, 2801 (1992).

[41]H. B. Yao, N. J. Zabusky, and D. G. Dritschel, ''High gradient phenomena in two-dimensional vortex interactions,'' Phys. Fluids **7**, 539 (1995).

[42]C. F. Driscoll, J. H. Malmberg, and K. S. Fine, ''Observation of transport to thermal equilibrium in pure electron plasmas,'' Phys. Rev. Lett. **60**, 1290 (1988).

[43]D. H. E. Dubin and T. M. O'Neil, ''Two-dimensional guiding-center transport of a pure electron plasma,'' Phys. Rev. Lett. **60**, 1286 (1988).